

Mass Lesion Detection in Mammographic Images using Haralik Textural Features

S. Tangaro¹, F. De Carlo¹, G. Gargano¹, R. Bellotti², U. Bottigli³, G. L. Masala⁴, P. Cerello⁵
S. Cheran⁶, R. Cataldo⁷, M. Quarta⁸ & E. Catanzariti⁹

¹Istituto Nazionale di Fisica Nucleare (INFN)-Bari, Italy

²Università and INFN di Bari, and Center of Innovative Technologies for Signal Detection and Processing, Italy

³Dipartimento di Fisica, Università di Siena and INFN-Cagliari, Italy

⁴Struttura Dipartimentale di Matematica e Fisica, Università di Sassari and INFN-Cagliari, Italy

⁵Istituto Nazionale di Fisica Nucleare-Torino, Italy

⁶Dipartimento di Informatica, Università di Torino and INFN - Torino, and ASP fellow, Italy

⁷Dipartimento di Scienza dei Materiali, Università di Lecce and INFN-Lecce, Italy

⁸Dipartimento di Matematica, Università di Lecce and INFN-Lecce, Italy

⁹Dipartimento di Scienze Fisiche, Università di Napoli and INFN-Napoli, Italy

In this work the implementation of a large mammographic database is described. The digitized images were collected since 1999 by a community of physicists in collaboration with radiologists in several Italian hospitals, as a first step to implement a Computer Aided Detection (CAD) system. The mammograms were collected from 967 patients; they were classified according to the type and the morphology of the lesions, the type of the breast tissue and the type of pathologies. Moreover we present a classification system for an automatic detection of masses in digitized mammographic images. The system consists in three main processing levels: (a) image segmentation for the localization of regions of interest (ROIs); (b) ROI characterization by means of textural features computed from the Gray Tone Spatial Dependence Matrix (GTSDM), containing second order spatial statistics information on the pixel grey level intensity; (c) ROI classification by means of a neural network, with supervision provided by the radiologist's diagnosis. The CAD system was developed and evaluated using a database of $N_t = 3369$ mammographic images: the breakdown of the cases was $N_n = 2307$ negative images, and $N_p = 1062$ pathological (or positive) images, containing at least one confirmed mass, as diagnosed by an expert radiologist. To examine the performance of the overall CAD system, receiver operating characteristic (ROC) and free-response ROC (FROC) analysis were employed. The area under the ROC curve was found to be $A_z = 0.78 \pm 0.008$ for ROI-based classification. When evaluating the accuracy of the CAD against the radiologist-drawn boundaries, 4.23 false positive per image (FPPI) are found at 80% mass sensitivity.

1. INTRODUCTION

The analysis of medical images is receiving, in the last years, a growing interest from the scientific community working at the crossover point among physics, engineering and medicine. The main purpose of this activity is to develop CAD systems for an automated search for pathologies, which could be of great help for the physicians' diagnosis.

A typical example is the analysis of mammographic images which are widely recognized as the only imaging modality for an early detection of breast neoplasia [1; 2]. Breast cancer is reported as the leading cause of woman cancer deaths in both United States and Europe. At present, screening programs are the best known method for an early diagnosis in asymptomatic women, thus allowing a reduction of the mortality [3, 4]. Screening programs are based on a double visual inspection of the mammographic images, as double reading was shown to increase diagnostic accuracy [5]. From this point of view, the use of a CAD system could provide valuable assistance to the radiologist.

In the present paper, a CAD system for mass detection will be described. The masses are often clear marks of a breast neoplasia. Masses are rather large ($d \simeq 1$ cm of diameter) objects with variable shapes, showing up with faint contrast. These textural characteristics can be exploited in both the definition of a ROI hunter procedure and the choice of the proper features to discriminate positive regions of the mammogram from negative ones.

This work fits in the more general framework of the MAGIC-5 Project (Medical Application on a Grid Infrastructure Connection) [7]. The image collection in a screening program intrinsically creates a distributed database, as it involves many hospitals and/or screening centers in different locations. The amount of data generated by such periodical examinations would be so large that it would not be efficient to concentrate them in a single computing center. As an example, let us consider a mammographic screening program to be carried out in Italy: it should check a target sample of about 6.8 millions women in the 49-69 age range at least once every two years, thus

implying a data flux of 3.4 millions mammographic exams/year. For an average data size of 50 MB/exam (4 images), the amount of raw data would be in the order of 160 TB/year. In addition, the amount of data linearly increases with time and a full transfer over the network from the collection centers to a central site would be large enough to saturate the available connections. On the other hand, making the whole database available to authorized users, regardless of the data distribution, would provide several advantages. This framework requires huge distributed computing efforts as for the case of the HEP (High Energy Physics) experiments, e.g. the CERN/LHC (Large Hadron Collider) collaborations. The best way to tackle these demands is to use the GRID technologies to manage distributed databases and to allow real time remote diagnosis. This approach would provide access to the full database from everywhere, thus making possible large-scale screening programs. The MAGIC-5 Project fits in this framework, as it aims at developing Computer Aided Detection (CAD) software for Medical Applications on distributed databases by means of a GRID Infrastructure Connection.

2. THE IMAGE DATABASE

A medical images dataset is considered the starting point for important studies such as a comparison of algorithms for training and testing of CAD systems. The mammograms used in this study were collected in a network of hospitals belonging to the MAGIC-5 collaboration [9,10]. Images were acquired using different mammographic screen/film systems and settings (all with molybdenum anode) and in the framework of different applications, including both clinical routine carried out on symptomatic women, and screening programs addressed to asymptomatic women. A workstation, composed of a PC running the Linux operating system and a film scanner, was installed at each site involved in the program. All the mammograms of the database were digitized using the same digitizer model and under the same conditions in order to avoid artificial features caused by variations in the digitization step. All the images were digitized with a CCD scanner at a pixel size of $85\mu\text{m} \times 85\mu\text{m}$ with 12 bits gray level resolution (4096 grey levels tones) [11]. The typical scan time is 20s. The acquisition software provided with the scanner was modified to scan and save images in a special format consisting of a long vector of numbers corresponding to the pixel intensities and two other numbers representing the image dimension. These numbers are used to transform the vector in a matrix: each pixel of the image can be represented by a triplet (x, y, I) , where x is the row number, y is the column number and I is the intensity of the pixel, ranging from 0 (black) to 4095 (white). Each image has a standard size of about 8 Mbytes. In sites where clinical studies were performed, the PC was connected to a high resolution and high luminosity B/W LCD monitor.

The database is composed of $N_i = 3369$ mammographic images, each including data and clinical information. Images

were collected from $n_s = 967$ patients, whose age ranges from 22 to 84. The age distribution is reported in figure 1.

Each patient has from one to six views (central, lateral, oblique), according to the distribution shown in figure 2. Different views from the same subject and are treated as different case samples in the analysis.

The pie diagrams reported in figure 3 shows the repartition of the database in left/right breast images (left) and craniocaudal/oblique/lateral views (right). The image size is 2067×2657 pixels.

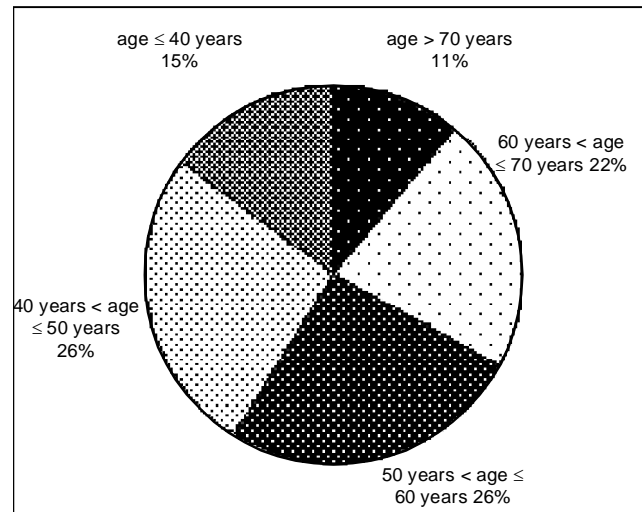


Figure 1: Age groups of the analyzed subjects

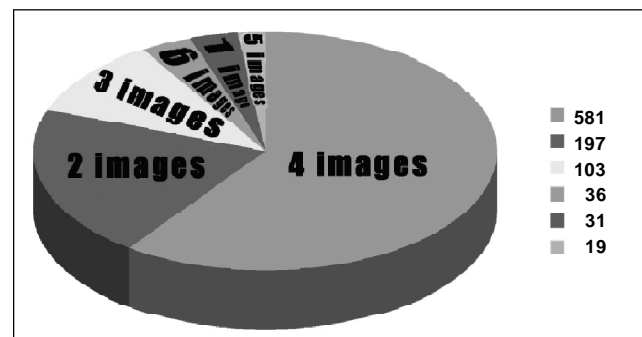


Figure 2: Number of cases with 1-6 images

All the mammographic images with other information related to the patient (follow up, age of patients and interesting cases) were collected in the Italian hospitals involved in the MAGIC5 collaboration. The geographic provenience of the images is shown in figure 4.

All the images of the database containing one (or more) lesions were characterized according to the kind of lesions (massive or microcalcification), its grade of malignancy, the kind of texture of the breast, etc. In this study there are the images from 306 patients who were defined normal when proven by three years of radiological follow up, or, generally, when there was no evidence of any lesion. The remaining images proceed from 661 "abnormal" patients: when a

suspicious lesion was found in these images, it was classified as suspicious; when more diagnostic procedures were carried out on the patient, the feature was identified as benign or malignant, according to the cytological or histological results.

We consider positive images the ones which contain at least one mass, as diagnosed by an expert radiologist and confirmed by biopsy; images with no mass at the first exam and after a follow up of at least three years are considered as negative, even if they contain some other pathology (e.g. microcalcifications). The breakdown of the cases is displayed in figure 5 for both the images (positive/negative) and the analyzed subjects (pathological/healthy).

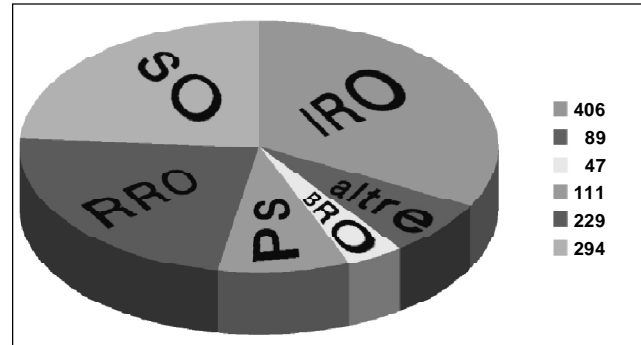


Figure 6: Different kinds of masses present in the database. Legend: IRO = Irregular Roundish Opacity; SO = Spiculated Opacity; RRO = Regular Roundish Opacity; PS = Parenchymal Distorsion; BRO = Blurred Roundish Opacity; OTHERS include a combination of the above mentioned kinds

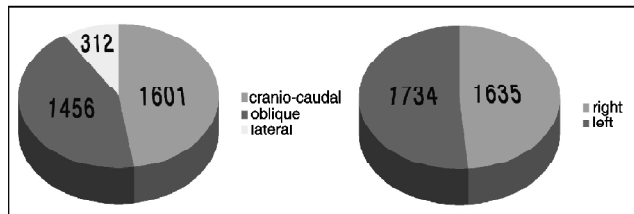


Figure 3: Database partition; left: number of left/right breast images; right: number of crano-caudal/oblique/lateral views

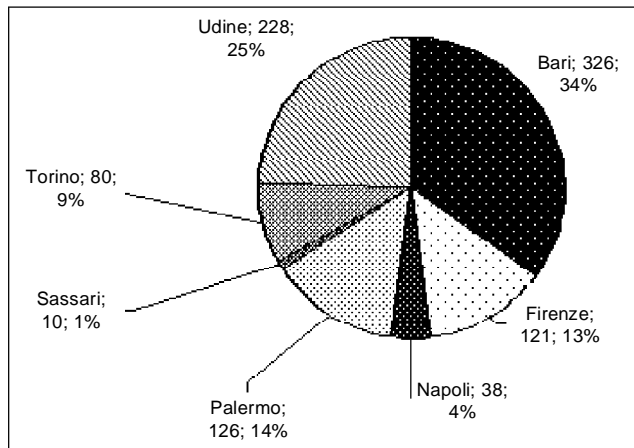


Figure 4: Geographic provenience of the images within MAGIC-5 database analyzed subjects (pathological/healthy)

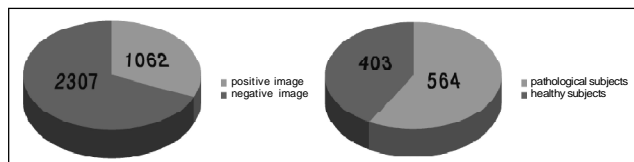


Figure 5: Database composition: images (left) and subjects (right)

In the database there are 1062 images containing at least one Region Of Interest (ROI) with a massive lesion and 304 images containing at least one ROI with microcalcifications. In total there are 1296 images containing at least one lesion, and 70 images contain both massive and microcalcification lesion.

The classification of breast background is based only on the appearance of the breast parenchyma. No consideration was given to the skin, vascularity, presence or absence of masses, calcifications, lymph nodes, nor to parity, history of breast disease, age, family history.

3. METHODS

It should be stressed that no kind of normalization is applied to the images.

The CAD system consists of three main steps: segmentation, feature extraction and classification. The goal of the segmentation step is to locate, within the images, those suspicious regions, or ROIs, which are more likely to contain a mass. All the detected ROIs will be characterized by a proper set of features providing a second-order spatial statistics information on the pixel intensity. It should be stressed that, in general, a number of ROIs can be detected with different degrees of superimposition on the same mass, though being not overlapped among them. In few words, ROI-to-mass is not a one-to-one mapping. A tagging criterion, relying on the superimposition with the radiologist-drawn boundary, is adopted to define the true positive (TP) ROIs. This procedure is necessary to train the neural network with a ground truth based on the radiologist’s diagnosis. Results are provided in terms of both ROC curve, displaying the neural network pattern (i.e. ROIs) classification and FROC curve, describing the overall CAD system (segmentation + feature extraction + neural network) mass detection performance.

In the following sections each of the above mentioned processing steps are reviewed.

3.1 Segmentation Methods

Prior to be processed, the images are made anonymous and the borders of the breast are extracted by means of a threshold algorithm whose accuracy has been visually verified case by case. In this way, non-interesting portions of the mammogram reporting information about right/left breast, examination date and so on has been cut off.

A segmentation algorithm has been implemented to select the suspicious regions of the mammogram. A detailed description of the ROI hunter, including the parameter selection, is given in [6]. Here we briefly provide the main points the algorithm is based on:

- the mammogram is divided into square cells of 200×200 pixels and a relative grey level maximum I_M (initial center for the candidate lesion) is searched in each cell;
- an iso-intensity contour, defining a ROI with area A_R which includes the relative maximum intensity pixel, is drawn for a certain initial threshold value $I_{th} = I_M/2$;
- the threshold is increased/decreased provided that the ROI area A_R is greater/smaller than a limit area A_L ; the iteration is stopped when the difference between two consecutive thresholds is less than 4 grey levels;
- the ROI is removed and stored for feature extraction and classification;
- the processing is repeated for the following square cell.

Figure 7 shows an example of the ROIs selected with the segmentation algorithm (right), together with the original image (left).

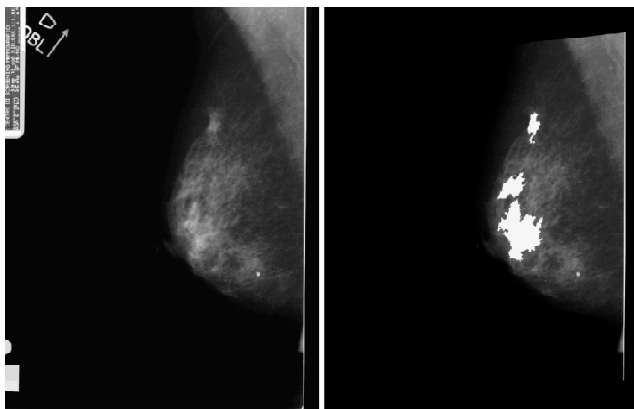


Figure 7: Left: the original image; right: the segmented image

The number of ROIs detected from each image is not set *a priori*, rather it is related also to the texture properties of the mammogram. All the ROIs extracted from negative images are tagged as negatives, while the ROIs from positive images can be labeled as true positive (TP) or false positive (FP), depending if they meet or not of the radiologist-drawn boundary.

We point out that for the following classification step only TP and negative ROIs are used for both training and testing the neural network, according to the cross-validation technique (see section 8), while the FP ones are used for validation purpose only.

The efficiency of the ROI hunter, computed as the percentage of masses correctly detected among those found by the radiologist, is 83.1%, corresponding to 1027 detected

masses, with respect to 1236 radiologist-drawn boundaries. Moreover, 6.27 FPPi are obtained at this level, and the average area of the selected ROIs is 15% of the total area of the image. Table 1 reports the breakdown of the selected ROIs.

Table 1
Breakdown of the selected ROIs

TP	FP	negative	total
1207	7642	13473	22322

3.2 Feature Extraction

Texture analysis can be used either to segment the image into areas indicating the mass, or to measure textural features to classify possible pathological sites. This approach has been used in [12] to experiment lung cancer nodule detection by means of textural features and neural network classification. This led us to follow a similar approach for the detection of the masses in mammography. The focus of the analysis is the computation of the Grey Level Co-occurrence Matrix (GLCM) [13], also known as Spatial Grey Level Dependence (SGLD) [14]. To this purpose, we consider the minimal rectangular portion of the image which fully includes the ROI. As the name suggests, the GLCM is constructed from the image by estimating the pairwise statistics of pixel intensity, thus relying on the assumption that the texture content information of an image is contained in overall or average spatial relationship between pairs of pixel intensities [13]. A co-occurrence matrix \mathcal{M} is a $G \times G$ matrix, whose rows and columns are indexed by the image grey levels $i = 1, \dots, G$, where $G = 2^n$ for an n -bit image. Each element p_{ij} represents an estimate of the probability that two pixels with a specified polar separation (d, θ) have grey levels i and j . Coordinates d and θ are, respectively, the distance and the angle between the two pixels i and j . In their seminal paper [13], Haralick *et al.* considered only displacements $d = 1$ at quantized angles $\theta = k\pi/4$, with $k = 0, 1, 2, 3$, thus having $\mathcal{M}_{d,\theta}(j, i) = \mathcal{M}_{d,\theta+\pi}(i, j)$. Symmetry is achieved by averaging the GLCM with its transpose, thus leading to invariance under π -rotations too. Textural features can be derived from the GLCM and used in texture classification in place of the single GLCM elements. In [13], 14 features are introduced, related to a textural property of the image such as homogeneity, contrast, presence of organized structure, complexity and nature of grey tone transitions. The values of these features are sensitive to the choice of the direction θ , given that the parameter d is fixed to 1 (greater values are rarely used). Invariance under rotation should be restored in order to avoid describing two images, one obtained by rotating the other, with different feature sets. This is achieved by considering mean and range of each feature values over the θ angles, thus obtaining a number of 28 textural variables, even if only few of them are used as inputs to a classifier [14, 15, 16].

As the texture is grey tone independent, either the image must be normalized or one should choose features which are invariant under monotonic grey level transformation. We select, among all GLCM features, the following features which are grey tone independent:

1. angular second moment:

$$f_1 = \sum_{ij} p_{ij}^2; \quad (1)$$

2. entropy:

$$f_2 = -\sum_{ij} p_{ij} \ln(p_{ij}); \quad (2)$$

3. information measures of correlation:

$$f_3 = \frac{f_2 - H_1}{\max\{H_x, H_y\}}; \quad (3)$$

$$f_4 = (1 - \exp\{-2(H_2 - f_2)\})^{1/2}, \quad (4)$$

where

$$P_x(i) = \sum_j p_{ij} \quad (5)$$

$$P_y(j) = \sum_i p_{ij} \quad (6)$$

$$H_1 = -\sum_{ij} p_{ij} \ln\{P_x(i)P_y(j)\} \quad (7)$$

$$H_2 = -\sum_{ij} P_x(i)P_y(j) \ln\{P_x(i)P_y(j)\} \quad (8)$$

$$H_x = -\sum_i P_x(i) \ln\{P_x(i)\} \quad (9)$$

$$H_y = -\sum_j P_y(j) \ln\{P_y(j)\} \quad (10)$$

For each of the above mentioned features $\{f_i\}$, ($i = 1, \dots, 4$), mean and range are computed over $\theta = k\pi/4$ angles, with $k = 0, 1, 2, 3$, thus obtaining a number of eight textural features. For illustrative purpose, let us focus on the f_1 variable to show the effectiveness of this variable to discriminate positive from negative ROIs. The angular second moment (ASM) is a measure of the grey tone homogeneity. In a quite homogeneous window (see fig. 8 (a) displaying not a suspicious region) there is a large number of few dominant grey tone transitions, giving few entries of great probabilities in \mathcal{M} , corresponding to high ASM values. On the other case (see fig. 8 (b) which refers to a mass), there is a larger number of transitions with low statistics, hence many entries with small probabilities in the co-occurrence matrix: this implies small ASM values for inhomogeneous windows. For the cases shown in fig. 8, both the mean and the range of the angular second moment are one order of magnitude different: $\langle f_1 \rangle = 0.0014$, $\text{range}(f_1) = 10^{-4}$ for the negative ROI, (fig. 8a), $\langle f_1 \rangle = 0.0001$, $\text{range}(f_1) = 10^{-5}$ for the positive ROI (fig. 8b).

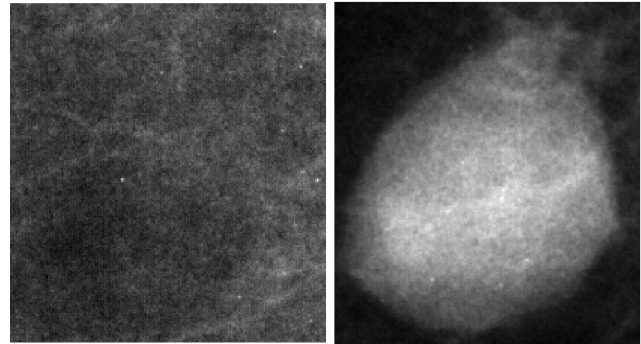


Figure 8: (a): negative ROI; (b): positive ROI

3.3 Classification

We used a supervised two-layered feed-forward neural network, trained with gradient descent learning rule [17] for the ROI pattern classification.

The network architecture consisted of $n_i = 8$ input neurons and one output neuron. The size of the hidden layer was tuned in the range $[n_i - 1, 2n_i + 1]$ to optimize the classification performance.

All the TP ROIs ($N_{TP} = 1207$) and as many negative ones were used to train the neural network. To make sure that the negative training patterns were representative, they were selected with a probability given by the distribution of the whole negative ROI set, in the eight-dimensional feature space. With a random procedure we build up two sets (A and B), each one made of 1207 patterns, which are used, in turn, for both training and test, according to the cross validation technique [19]: first, the network is trained with set A and tested with set B, then the two sets are reversed. All the other patterns (negative ROIs not selected for the training stage and FP) are used for validation only. The results presented in the following section (see ROC curves in section 2) refer to the classification of all the patterns at our hand. The breakdown of the patterns for the cross validation is reported in table 2.

Table 2
Breakdown of the Patterns for the Cross Validation: First Set A is used for Training and set B for Testing, then Viceversa

	<i>set A</i>	<i>set B</i>	<i>validation</i>
TP ROI	603	604	/
negative ROI	604	603	13473
FPROI	/	/	7642
total	1207	1207	21115

In all run set A and set B contains a balanced number of both the considered type of masses and the different kinds of tissue.

4. RESULTS AND DISCUSSION

The performance of the neural stage is provided in terms of ROC curve [20] analysis. The ROC curve is particularly

suitable when testing a binary hypothesis: it is obtained by plotting the sensitivity (s , positive cases correctly recognized) against the false positive rate (FPR: fraction of misclassified negative patterns), at different values of the decision threshold.

In each case the classifications parameter (hidden neurons number, α) were changed so as the optimum performance was achieved.

Figure 9 displays a typical ROC curve obtained for the pattern classification. The area under the curve (AUC) is $A_z = 0.783 \pm 0.008$, where the error is computed as reported in Hanley *et al.* [21]. The results are quite insensitive to the number N_h of the hidden neurons and α parameter.

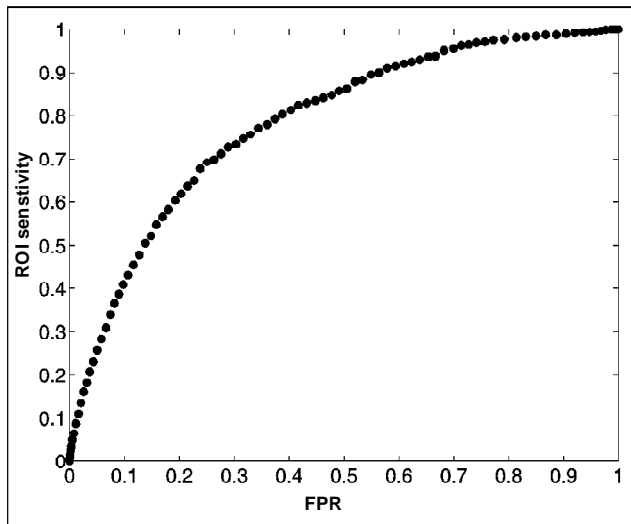


Figure 9: ROC curve for ROI-based classification. The area under the curve (AUC) is $A_z = 0.783 \pm 0.008$

As said in section 3, a number of ROIs can be superimposed to the same mass though not overlapping among them. For this reason, it should be more useful to provide the results in terms of the mass sensitivity, defined as the fraction of masses correctly detected by the CAD with respect to the total number of radiologist-drawn boundaries. In this way, the accuracy of the overall CAD system can be assessed against the radiologist's diagnosis. To this purpose, the following prescription is adopted: a mass is correctly detected by the CAD system if at least one ROI, among the ones superimposed to that mass, is classified as positive by the neural network.

A free-response ROC (FROC) curve can be drawn (see figure 10), which reports the mass sensitivity of the overall system against the number of false positive per image (FPpI): 80% of mass sensitivity is achieved with 4.23 FPpI.

5. CONCLUSIONS

The database collected represents a useful archive of digitized mammographic images. It can be a valuable tool to the scientific community for different tasks such as training and testing of Neural Network based classification tools [22, 23, 24, 25]. A three-level classifier was developed and

tested on the above described database. The first level is a segmentation-based procedure to extract ROIs. This routine consists in a dynamical threshold algorithm which allows to select iso-intensity contours around grey level maxima of the mammogram. The second level performs the feature extraction, based on the use of eight grey tone independent textural features measured from the GTSD matrix: these features carry second order spatial statistics information on the pixel intensity of the suspicious regions. The third level does the final classification by means of a two-layered feed-forward supervised neural network.

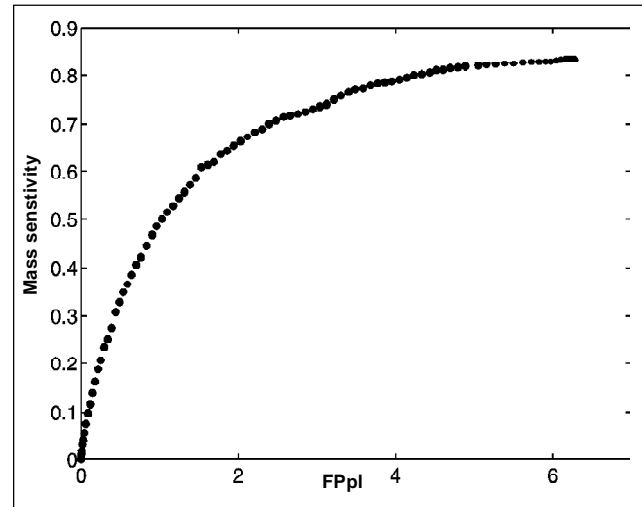


Figure 10: CAD FROC curve for mass-based classification

The results are provided in terms of ROC curve for the ROI-based neural classification, and FROC curve for the mass-based CAD classification.

Our scheme was developed and evaluated on a large database of mammographic images collected in the hospitals belonging to the MAGIC-5 Collaboration. The breast masses contained in the database span a wide range of shapes, sizes, and contrasts.

Like in a screening program, data are collected from geographically remote sites. The growth of the database and the distributed nature of the collaboration raises a problem, since images are generally not replicated between remote sites. The approach used to solve the problem of remote access was to use techniques developed for GRID computing [26,27].

6. ACKNOWLEDGMENTS

We acknowledge the help of the staff and the institutions involved in the study. In particular, we thank prof. V. Lattanzio (Policlinico di Bari, Italy), prof. Bazzocchi (Dipartimento di Ricerche Mediche e Morfologiche, Università di Udine, Italy), prof. E. Zanon (Ospedale Valdese di Torino and INFN, sezione di Torino, Italy), prof. A. Sodano (Dipartimento di Scienze Biomorfologiche e Funzionali, Università Federico II, Napoli, Italy) and Prof. R. Lagalla, Dr. R. Ienzi (Istituto di Radiologia P. Cignolini,

Università di Palermo) for the medical support in the data acquisition.

REFERENCES

- [1] L. W. Bassett, *et al.*, "History of the technical development of mammography, Syllabus: A Categorical course in Physics", RSNA (1994).
- [2] L. Tabar, *et al.*, "Reduction in mortality from breast cancer after mass screening with mammography randomised trial from the Breast Cancer Screening Working Group of the Swedish National Board of Health and Welfare", *Lancet* 829, 8433 (1985).
- [3] S. Feig, "Increased benefit from shorter screening mammography intervals for women ages 40-49 years", *Cancer* 80, 2035-2039 (1997).
- [4] R. Bird, *et al.*, "Analysis of cancer missed at screening mammography", *Radiology* 184, 613-617 (1992).
- [5] N. Karssemeijer, *et al.*, "Computer-aided detection versus independent double reading of masses in mammograms", *Radiology* 227, 192-200 (2003).
- [6] F. Fauci, *et al.*, "Mammogram Segmentation by Contour Searching and Massive Lesion Classification with Neural Network", *Proc. IEEE -Transaction on Nuclear Science*, 53(4), (2006).
- [7] R. Bellotti, *et al.*, "The MAGIC-5 Project: Medical Applications on a Grid Infrastructure Connection", *Proc. IEEE Nuclear Science Symposium*, October 16-22 2004, Rome, Italy.
- [8] C. S. Cheran, *et al.*, "Detection and Classification of Microcalcification Clusters in Digital Mammograms", *Proc. IEEE Medical Imaging Conference*, October 16-22 2004, Rome, Italy.
- [9] M. Bazzocchi, *et al.*, "Application of a computer-aided detection (CAD) system to digitalized mammograms for identifying microcalcifications", *Radiol. Med.* 101, 334-340 (2001).
- [10] M. E. Fantacci, *et al.*, "Search of microcalcifications clusters with the CALMA CAD Station", *Physics of the Medical Imaging*, San Diego, USA, February 24-26, 2002.
- [11] S. R. Amendolia *et al.*, "Comparison of imaging properties of several digital radiographic system", *Nuclear Instruments and Methods in Physics Research A* 466, 95-98 (2001).
- [12] G. S. Cox, F. J. Hoare, G. de Jager, "Experiments in lung cancer nodule detection using texture analysis and neural network classifiers", in *Third South African Workshop on Pattern Recognition*, 1992.
- [13] R. M. Haralik, K. Shanmugam, I. Dinstein, "Textural Features for Image Classification", *IEEE Transactions on Systems, Man and Cybernetics*, Vol. SMC-3, 610-621 (1973).
- [14] R. W. Connors and C. A. Harlow, "A Theoretical Comparison of Texture Algorithm", *IEEE Transactions on Pattern Analysis and Machine Intelligence* 2, 204-222 (1980).
- [15] R. W. Connors, *et al.*, "Segmentation of a High-Resolution Urban Scene using Texture Operators", *Computer Vision, Graphics and Image Processing* 25, 273-310 (1984).
- [16] J. S. Weszka, C. R. Dyer, and A. Rosenfeld, "A Comparative Study of Texture measures for Terrain Classification" *IEEE Transactions on Systems Man and Cybernetics* 6, 269-285 (1976).
- [17] J. Hertz, A. Krogh and R.G. Palmer, "Introduction to the theory of neural computation", *Addison-Wesley* (1991).
- [18] D. E. Rumelhart and J. L. McClelland, "Parallel Distributed Processing" Vol.I MIT Press, Cambridge, MA (1986).
- [19] M. Stone, "Cross-validatory choice and assessment of statistical predictions", *Journal of the Royal Statistical Society B* 36 (1), 111-147 (1974).
- [20] J. A. Swets, "Measuring the accuracy of diagnostic systems", *Science* 240, 1285-1293 (1988).
- [21] J. A. Hanley and B. J. McNeil, "The Meaning and Use of the Area under a Receiver Operating Characteristic (ROC) Curve", *Radiology* 143, 29-36 (1982).
- [22] S. Bagnasco, R. Bellotti, D. Cascio, S. C. Cheran, G. De Nunzio, M. E. Fantacci, F. Fauci, G. Forni, A. Lauria, E. Lopez Torres, R. Magro, G.L. Masala, P. Oliva, M. Quarta, G. Raso, A. Retico, S. Tangaro, "Mammogram segmentation by contour searching and massive lesions classification with Neural Network"; *IEEE-Transactions on Nuclear Science (TNS)* 53(4), (2006).
- [23] Bellotti R., De Carlo F., Gargano G., Maggipinto G., Tangaro S., Castellano M., Massafra R., Cascio D., Fauci F., Magro R., Raso G., Lauria A., Forni G., Bagnasco S., Cerello P., Cheran S. C., Lopez Torres E., Bottigli U., Masala G. L., Oliva P., Retico A., Fantacci M. E., Cataldo R., De Mitri I., De Nunzio G. "A completely automated CAD system for mass detection in a large mammographic database"; *Medical Physics*, 33(8), 3066-3075, (2006).
- [24] F. Fauci, G. Raso, R. Magro, G. Forni, A. Lauria, S. Bagnasco, P. Cerello, S. C. Cheran, E. Lopez Torres, R. Bellotti, F. De Carlo, G. Gargano, S. Tangaro, I. De Mitri, G. De Nunzio, R. Cataldo: A massive lesion detection algorithm in mammography; *PhysicaMedica*, XXI(1), 21-28, (2005).
- [25] G. Masala, S. Tangaro, M. Quarta, S. C. Cheran, E. L. Torres. "Classifiers trained on dissimilarity representation of medical pattern: a comparative study"; *Il Nuovo Cimento C*, Volume 028, Issue 06, 905-912.
- [26] S. Bagnasco, U. Bottigli, P. Cerello, S. Cheran, P. Delogu, M. E. Fantacci, F. Fauci, G. Forni, A. Lauria, E. Lopez Torres, R. Magro, G. L. Masala, P. Oliva, R. Palmiero, L. Ramello, G. Raso, A. Retico, M. Sitta, S. Stumbo, S. Tangaro, E. Zanon. "GPCALMA: a GRID based tool for mammographic screening; *Methods of Information in Medicine*"; n. 2, 244-248, (2005).
- [27] R. Bellotti, P. Cerello, V. Bevilacqua, M. Castellano, G. Mastronardi, S. Tangaro, F. De Carlo, S. Bagnasco, U. Bottigli, R. Cataldo, E. Catanzariti, S. C. Cheran, P. Delogu, I. De Mitri, G. De Nunzio, M. E. Fantacci, F. Fauci, G. Gargano, B. Golosio, P. L. Indovina, A. Lauria, E. Lopez Torres, R. Magro, G. L. Masala, R. Massafra, P. Oliva, A. Preite Martinez, M. Quarta, G. Raso, A. Retico, M. Sitta, S. Stumbo, A. Tata, S. Squarcia, A. Schenone, E. Molinari, B. Canesi. "Distributed Medical Images Analysis on a Grid Infrastructure"; *Future Generation Computer System, Special Issue on Life Science Grids for Biomedicine and Bioinformatics*, 23/3, 475-484, (2006).